Journal of Materials Chemistry A

ROYAL SOCIETY OF CHEMISTRY

PAPER

View Article Online
View Journal

Cite this: DOI: 10.1039/d5ta06204g

Discovery of two new Cu–Sn chalco–halides for potential solar absorber applications

Brinda Kuthanazhi,[a] Debalina Banerjee,[b] Dmitry Maslennikov,[b] Andrij Vasylenko,[a] Jan P. Scheifers,[a] Cara J. Hawkins,[a] Daniel Ritchie,[a] Craig M. Robertson,[a] Marco Zanella,[a] Troy D. Manning,[a] Luke M. Daniels,[a] Marina R. Filip,[b] Matthew S. Dyer,[a] Laura M. Herz,[b] John B. Claridge[a] and Matthew J. Rosseinsky *[a]

We explore multiple-cation chalco–halide phase fields evaluated by their synthetic accessibility using machine learning models. Exploratory synthesis guided by computational tools leads to the discovery of two new compounds; $CuSn_2SI_3$ and $Cu_{0.35}Sn_{5.29}S_2I_7$, their structures, and electronic and optical properties are reported herein. This is the first report of a stable quaternary compound in the Cu–Sn–S–I phase field. The two new compounds show related crystal structures where $Sn_4S_2I_4$ layers are a common structural motif in both. These $Sn_4S_2I_4$ layers are connected by Cu_2I_2 layers and disordered Cu–Sn–I layers, forming the three-dimensional structures of $CuSn_2SI_3$ and $Cu_{0.35}Sn_{5.29}S_2I_7$ respectively. Electronic band structure calculations using density functional theory show the presence of a direct band gap in $CuSn_2SI_3$ and suggest anisotropic transport, in line with the layered structure of the compound. A mixture of the two compounds with ~86% $CuSn_2SI_3$, shows a band gap in the visible region, close to 2.1 eV and a significant photo-induced charge carrier mobility of ~1.3 $cm^2\ V^{-1}\ s^{-1}$. This demonstrates Cu–Sn chalco–halides can form a promising phase space to explore for solar absorber materials, with further design and tuning of band gap.

Received 31st July 2025
Accepted 14th March 2026

DOI: 10.1039/d5ta06204g

rsc.li/materials-a

Introduction

The need for efficiently and sustainably harvested solar energy to meet the rising energy requirements of humankind is paramount. In recent years, lead halide perovskites and related materials have attracted the attention of multidisciplinary researchers, and have emerged among leading candidate materials for future energy applications,[1–4] demonstrating a dramatic increase in power conversion efficiencies over the last decade.[5,6] While their low cost of production from simple solution-based methods[7] and the excellent device performance make them attractive for commercial applications, the presence of the toxic element lead (Pb) and the poor long term stability of these materials, which often incorporate organic cations, have been limiting factors in their development.[8–10] Replacing Pb^{2+} with isoelectronic Sn^{2+} or Ge^{2+} in the halide perovskites, while reducing toxicity, compromises stability even further.[8] However, the presence of the heavy s^2 cation has been found to be critical in ensuring high performance,[11,12] by giving rise to electronic energy levels that are tolerant to high defect concentration. In addition to this, effective application of lead halide materials in devices, especially as multijunction solar cells, requires multiple materials with strong absorption onsets at different energies within the solar spectrum.

Multiple anion compounds, especially those that contain chalcogenide and halide anions (chalco–halides) have emerged as promising materials for various applications, due to the additional flexibility in tuning the chemical structure, dimensionality and material properties that the different anions provide.[13,14] In the context of solar absorbers, these materials are expected to be more stable than halides because of the stronger covalent bonds formed by the chalcogenide anions, thus providing a way to improve the stability of halide-based materials while retaining their excellent absorption and optical properties.[15] However, most of the chalco–halides studied for solar absorber applications are lower dimensional ternary compounds[16] (*e.g.* SbSI,[17] BiSeI,[18] *etc.*). Such a reduction in dimensionality in two-dimensional (2D) or one-dimensional (1D) structures tends to give rise to less dispersive electronic bands, leading to lower charge carrier mobilities. Conversely, such flat bands could also lead to high absorption coefficients, arising from the high density of states near the band gap, or formation of tightly bound excitons due to quantum confinement.[19–21] Exploration of the chalco–halide chemical space could offer additional degrees of freedom to control the electronic and structural dimensionality to maximise both absorption as well as charge carrier mobilities.

[a]Department of Chemistry, Materials Innovation Factory, University of Liverpool, Liverpool L7 3NY, UK. E-mail: M.J.Rosseinsky@liverpool.ac.uk
[b]Department of Physics, University of Oxford, Oxford OX1 3PU, UK

Several copper containing compounds, especially chalcogenides, such as Cu_2ZnSnS_4 (CZTS) and $CuIn_xGa_{1-x}Se_2$ (CIGS) are established solar absorber materials. One of the reasons these materials are promising for optoelectronic applications is due to the ability of low valence, d^{10} cations such as Cu^+, Ag^+, *etc.* to promote defect tolerance by formation of shallow defects.[11,22–25] Chalco–halide materials containing multiple cations, particularly d^{10} cations are highly underexplored for solar absorber applications,[15] with $CuBiSCl_2$ being a notable exception, and the combination of multiple anions could enable access to more diverse structure types and offer greater control of material properties. Other known quaternary chalco–halides with a d^{10} and an s^2 cation often contain the Bi^{3+} cation. Only a handful of other s^2 cation containing quaternary compounds are known including $CdSnSX_2$ (X = Cl, Br),[26] $Hg_2PbS_2I_2$,[27] $Cu_5SbS_3I_2$,[28] $CdSbS_2X$ (X = Cl, Br),[29] *etc.* Exploration of such space thus presents an opportunity to identify new and potentially functional materials.

In this article we report on the synthetic exploration of Cu containing chalco–halide phase fields, guided by computational tools and the discovery of two new quaternary compounds. We investigate the structure, optical properties, and electronic band structure of $CuSn_2SI_3$ to evaluate its performance as a candidate solar absorber material.

Experimental and computational methods

Determining phase fields

An unsupervised machine learning algorithm, based on a variational autoencoder (VAE) was used to assess the synthetic accessibility of the phase fields, similarly to the approaches developed in ref. 30 and 31. We first select compounds for which a finite (non-zero) band gap is reported in the materials platform for data science (MPDS) database[32] resulting in 68 823 entries. The phases were then aggregated into phase fields, *i.e.*, Ag_3AlF_6 and $AgAlF_4$ represent the same phase field Ag–Al–F, which resulted in 40 785 unique phase fields as the training data, which introduces a bias towards elemental combinations exhibiting a finite band gap (Fig. S1).

Two VAE models were built based on different schemes for element descriptions – Mat2Vec[33] and Local structure-induced Atomic Features (LEAFs)[30] – reflecting knowledge of their existence and characteristic structural motifs of local atomic environment, respectively. During training, the VAE reduces the dimensionality of the 200- and 37-dimensional elemental descriptors, for Mat2Vec and LEAFs respectively, aligning similar values in the latent space, and through such encoding and decoding learns the patterns of elemental combinations characteristic of the synthetic accessibility.

The candidate phase fields consisted of all possible combinations of the elements Cu-M-Ch-X-X′with M being a cation with s^2 electronic configuration among Sn, Bi, Pb, and Sb, and Ch stands for the chalcogen anion S or Se, X are halide anions among F, Cl, Br, and I, and X′ was from {Ch, X}, which are then subjected to the trained VAEs for ranking: the lower the score the more similar is the combination to the training data in the latent space of the model, and we hypothesise it is more likely to be synthetically accessible, *i.e.* more likely to contain synthetically stable compounds.

Points distribution algorithm

The points distribution algorithm attempts to evenly space out suggested compositions whilst avoiding known phases in a phase field.[34] The phase field is first discretised using a 2D orthogonal grid of approximately 500 points spanning all charge balanced compositions. A Markov Chain Monte Carlo (MCMC) method is then used to identify a suitable solution consisting of a small subset (five) of these points. At the heart of the MCMC method is the function used as a proxy to the energy which is used to evaluate how good a solution is. The proxy energy function attempts to jointly maximise all pairwise distances between suggested points as well as all pairwise distances between suggested points and known phases. The MCMC method begins with a random initial distribution of points. This distribution is then perturbed by randomly updating a selection of the points to new positions. The new distribution is then accepted with a probability based on the improvement in the proxy energy function. The process is then repeated 50 000 times, and the best distribution obtained during the entire run is used as the initial sampling suggestion. For this solution, the discrete grid is constrained to exclude any compositions with less than 5% (molar) of either copper or tin.

Exploratory synthesis

The initial compositions as suggested by the points distribution algorithm, equally spaced out from each other and known compounds were: C0–$Cu_{2.44}Sn_{1.13}S_{2.27}I_{0.16}$, C1–$Cu_{1.68}Sn_{1.74}S_{2.58}$, C2–$Cu_{0.63}Sn_{2.31}S_{2.19}I_{0.87}$, C3–$Cu_{1.98}Sn_{0.95}S_{0.81}I_{2.26}$, and C4–$Cu_{1.81}Sn_{1.29}S_{1.49}I_{1.41}$. The precursors used were copper(I) iodide (CuI, 99.998% metals basis, Puratronic), copper(I) sulfide (Cu_2S, 99.5% metals basis, Thermofisher Scientific), tin(II) iodide (SnI_2, ultra dry, 99.999% metals basis, Thermofisher Scientific), and tin(II) sulfide (SnS, 99.5%, Thermofisher Scientific). The precursors were weighed out in the required stoichiometry of the chosen initial compositions and ground well to mix using a mortar and pestle, inside an argon-filled glovebox. The ground mixtures were then sealed in evacuated quartz tubes and heated to a temperature of 400 °C (T_1), at a rate of 5 °C per minute. After dwelling at 400 °C for 12 hours, the reactions were slowly cooled down to room temperature at a rate of 6.3 °C h^{-1}. A similar set of reactions were carried out with the same initial compositions, and protocol but with the temperature set to 600 °C (T_2) at a rate of 5 °C per minute. After dwelling at 600 °C for 12 hours, the reactions were slowly cooled down to room temperature at a rate of 6.3 °C h^{-1}. Finally, a third set of reactions were run at 700 °C (T_3). The lowest temperature of 400 °C was chosen such that it is above the melting point of SnI_2 (320 °C) to aid reaction of the precursors. Subsequent higher temperatures were chosen to facilitate melting of the rest of the precursors with higher melting temperatures while remaining below the boiling point of SnI_2 (714 °C), to avoid issues with possible over pressurization of the ampoule and loss of iodides. The reactions were

labelled using the initial composition and the temperature used, *e.g.*, C1T3 for initial composition C1–$Cu_{1.68}Sn_{1.74}S_{2.58}$ run at the temperature T_3–700 °C.

Powder X-ray diffraction (XRD) was carried out on all fifteen samples, and single crystals were harvested from the reactions that had highest intensity of unindexed peaks (C3T2 and C4T3). Single crystal X-ray diffraction studies on such crystals, revealed two new structures – $CuSn_2SI_3$ and $Cu_{0.35}Sn_{5.29}S_2I_7$. Once the two new structures were solved, the powder X-ray diffraction patterns of all the exploratory reactions could be satisfactorily fitted with a mixture of precursors, known ternaries and binaries, and the two new structures, indicating no other new compounds have been formed with the compositions and reaction conditions we used. The reaction products of exploratory syntheses were mixtures of various known and newly found phases, not single phase pure compounds. This is expected as the initial compositions were predicted for exploration and not as target compositions, and conditions were not optimised. With the compositions obtained from single crystal XRD, we attempted to synthesise $CuSn_2SI_3$ and $Cu_{0.35}Sn_{5.29}S_2I_7$ as high purity powders *via* solid state synthesis.

Solid state synthesis of $CuSn_2SI_3$

The precursors CuI, SnI_2, and SnS were weighed out in the molar ratio 1 : 1 : 1, and ground well to form a homogenous mixture using a mortar and pestle, in an argon filled glovebox. The powder was then pressed into a 10 mm pellet using a stainless-steel die and a uniaxial press with a weight of 2 tons for about 1 minute. The pellet was then sealed in an evacuated quartz tube and heated up to 250 °C with a rate of 60 °C h^{-1}. After dwelling at 250 °C for 24 hours, it was slowly cooled down to room temperature at a rate of 5 °C h^{-1}. This resulted in a mixture of $CuSn_2SI_3$, $Cu_{0.35}Sn_{5.29}S_2I_7$, and unreacted SnI_2. Hence the process was repeated with intermediate grinding and pelletizing, as well as with increasing dwell time at 250 °C to one week. After three repeated reactions the products formed were ~85% (by weight) $CuSn_2SI_3$ as estimated from powder XRD. Further firing of the reaction did not make any discernible difference in the purity. Attempts to make $Cu_{0.35}Sn_{5.29}S_2I_7$ by similar methods always resulted in a mixture of phases-$Cu_{0.35}Sn_{5.29}S_2I_7$, $CuSn_2SI_3$, and unreacted precursors, with samples containing <70% $Cu_{0.35}Sn_{5.29}S_2I_7$. Hence, we did not carry out any optical property measurements on $Cu_{0.35}Sn_{5.29}S_2I_7$.

Powder samples prepared through solid state synthesis were ball milled in a planetary ball mill with a zirconia pot and 5 mm diameter balls (1 : 10 weight for sample to balls), at 300 rpm for 20 minutes, to obtain particle sizes of several micron. Powder XRD and energy dispersive X-ray spectroscopy (EDX) confirmed non-degradation of sample in the process. The milled powder was used for making cold pressed pellets and used for terahertz spectroscopy measurements.

Single crystal X-ray diffraction

X-ray diffraction measurements on orange-red, needle shaped, single crystals picked from the exploratory synthesis attempts C3T2 and C4T3 were carried out in-house using a Rigaku MicroMax-007 HF X-ray diffractometer equipped with a Mo K_α rotating-anode microfocus source and a Saturn 724 + detector. The measurements were performed with the sample at 300 K for $CuSn_2SI_3$ and at 100 K for $Cu_{0.35}Sn_{5.29}S_2I_7$. Cell refinement and data reduction were performed using the CrysAlis^{Pro} software. The structure was solved and refined using SHELX,[35] implemented through Olex2.[36] The crystal structures were visualised using the software VESTA[37] for creating the images.

Powder X-ray diffraction

Preliminary phase identification of powder samples was done using powder X-ray diffraction using an in-house Rigaku Smartlab diffractometer with a Mo K_α source ($\lambda = 0.7107$ Å) in the Debye–Scherrer geometry. Powder samples were sealed in 0.3 mm diameter borosilicate capillaries inside an Ar-filled glovebox for measurements. Synchrotron powder X-ray diffraction measurements were carried out at the beamline I11 at the Diamond Light source, Didcot,[38] UK. Rietveld refinement on powder XRD data was carried out using TOPAS Academic V5 software.

UV-visible spectroscopy

UV-visible spectra on powder samples were measured using an Agilent Cary 5000 spectrometer in the diffuse reflectance mode. The reflectance data were transformed using Kubelka–Munk equations to obtain absorption data.

Scanning electron microscopy (SEM)

Imaging and EDX measurements were done on a Tescan S8000 microscope using a X-Max^N detector from Oxford instruments. Powder and crystals were mounted on an aluminium stub using a carbon tape. The sample was coated using carbon to avoid charging. Analysis of EDX spectra was done using Aztec software.

X-ray photoemission spectroscopy (XPS)

X-ray photoemission spectra on powder samples were measured at HarwellXPS, Didcot, UK. Measurements were carried out using a Kratos Axis SUPRA XPS fitted with a monochromatic Al K_α X-ray source ($h\nu = 1486.6$ eV), a spherical sector analyzer, and 3 multichannel resistive plate, 128 channel delay line detectors. All data were recorded at 150 W and a spot size of 700 × 300 μm^2. Survey scans were recorded at a pass energy of 160 eV, and high-resolution scans were recorded at a pass energy of 20 eV. Electronic charge neutralization was achieved using a magnetic immersion lens. All sample data were recorded at a pressure below 10^{-8} Torr and temperature of 294 K. Data were analysed using CasaXPS v2.3.26PR1.0. The background was fitted using a Shirley background and peaks fitted using a Gaussian–Lorentzian (GL(50)) peak shape. The spectra were calibrated with respect to the Fermi edge of a Ni foil reference.

First principles studies

First principles density functional theory (DFT)[39,40] calculations, as implemented in the plane-wave basis code Quantum

Espresso,[41,42] were carried out for the primitive cell of $CuSn_2SI_3$. The PBE exchange correlation functional[43] was used with norm-conserving fully relativistic Vanderbilt pseudopotentials[44] as available in the PseudoDojo database.[45] We used kinetic-energy and charge-density cutoffs of 100 Ry and 400 Ry, respectively. We performed unconstrained variable-cell relaxations on the experimentally measured structure using a uniform Γ-centred k-point grid of $8 \times 8 \times 3$ after which the unit cell volume expanded by 11% (see Table. S10), without significant changes to the relative atomic positions as compared to the unrelaxed structure. We note that structural optimisation with PBEsol yields a unit cell volume in better agreement with the experimental structure than that obtained using standard PBE (2% *vs.* 11%, respectively). However, a comparison of computed band structures for both the experimental and PBE relaxed structures (see SI Fig. S12), shows relatively minimal differences in the conduction and valence band edge states. Subsequent calculations presented in the main manuscript are performed on the PBE relaxed structure. We compute the density of states using a uniform $16 \times 16 \times 6$ k-point grid (772 irreducible k-points), including spin–orbit coupling (SOC). The effective mass tensor is calculated as the inverse of the second derivative of the energy with respect to the wave-vector, with derivatives being calculated using the finite difference method with a 5-point stencil and an optimised increment of 0.01 $Bohr^{-1}$. The effective mass tensor is computed and diagonalised using the effective mass calculator (emc) code.[46,47] We also included spin–orbit coupling for the relaxed structure using a q-point grid and k-point grid of $4 \times 4 \times 2$.

Charge-carrier mobility measurements

The effective electron–hole sum mobility at THz frequencies was measured using the optical-pump terahertz-probe (OPTP) method for a pressed pellet of $CuSn_2SI_3$ of known thickness (See SI for full details of the experimental technique and data analysis). In the OPTP method, charge carriers are photoexcited in a semiconductor with ultrafast laser pulses (wavelength $\lambda = 400$ nm), and the corresponding change in conductivity is measured through changes in the transmission of a single-cycle terahertz pulse. A value for the electron–hole sum mobility may be extracted from such data, provided the initial charge-carrier excitation density is known.[48–50] The pellet of $CuSn_2SI_3$ was pressed at room temperature using the pre-synthesized powder described above to achieve uniform densification. The resulting pellet measured 0.49 mm in thickness, 5 mm in diameter, and had a mass of 51.9 mg, corresponding to a calculated density of approximately 5.40 g cm^{-3}.

Results and discussion

Computationally guided phase field determination and exploration

We employ a computationally guided approach to identify the previously unexplored phase field of Cu–Sn–S–I as promising and explore it experimentally resulting in the discovery of two new compounds. This was attained through a two-step process.

1. Identifying Cu–Sn–S–I phase field. Using chemical knowledge and promising characteristics for solar absorbers, we first select a subset of element combinations denoted as Cu-M-Ch-X′-X, with M being a cation with s^2 electronic configuration among Sn, Bi, Pb, and Sb, and Ch stands for the chalcogen anion S or Se, X are halides anions among F, Cl, Br, and I, and X′ was from {Ch, X}. This way we incorporated an s^2 and a d^{10} cation, known for imparting defect tolerance, while two cations provide greater extent of tuneability. The choice of chalco–halide compounds was inspired by the fact that many ternary lead and tin halides have shown excellent optical absorption and charge carrier mobilities, but poor stability in ambient atmosphere/moisture. The addition of chalcogen anions to these halides are known to improve the stability. With this element selection, there still is a large number of choices to explore, and we used an unsupervised machine learning algorithm, based on a variational autoencoder (VAE) to assess the synthetic accessibility of the phase fields, similarly to the approaches developed in ref. 30 and 31. This algorithm ranks the candidate fields with its likelihood to have a stable compound. The candidate phase fields, Cu-M-Ch-X-X′, were subjected to the trained VAEs for ranking. A Pareto front optimising the results of the two VAE models we used (Mat2Vec and LEAFs, see methods for details) is shown in Fig. 1 for Ch = S.

Among the ranked test fields according to both models, the top five combinations contained Sn^{2+}. Chloride containing combinations were also consistently found higher ranked than other halides. We selected a quaternary phase field derived from the top ranked quinary candidate Cu–Sn–S–I–Cl phase field (circled in Fig. 1) in order to begin experimental investigation. The four-element field Cu–Sn–S–I does not have any reported quaternary compounds and is among the less explored fields with a low number of known ternaries and thus was chosen for exploratory synthesis attempts. The known ternary compounds in this phase field are listed in Table S1.

2. Exploratory synthesis to identify new compounds. Once the phase field was chosen, we need to explore it in a systematic manner, by attempting synthesis with varying initial composition and reaction conditions. A points distribution algorithm was used to suggest five plausible initial compositions for experimental synthesis within the quaternary cut of the phase space as restricted by the choice of precursors – Cu_2S, CuI, SnI_2, and SnS. The algorithm ensures that the separation between these five compositions and from the precursors is maximised whilst also avoiding known phases. These five compositions, C0–C4, were weighed out and reacted at different temperatures (see Methods). After this, all products were analysed with powder X-ray diffraction. Samples which had unidentified peaks were then subject to single crystal XRD, where numerous single crystals from each batch were screened to find a unit cell not reported in ICSD. Two new structures were discovered this way, with the compositions of $CuSn_2SI_3$ and $Cu_{0.35}Sn_{5.29}S_2I_7$.

Structure determination and description

The crystal structure of $CuSn_2SI_3$ (Fig. 2) was solved from single crystal X-ray diffraction data with $C2/m$ (#12) symmetry, and unit

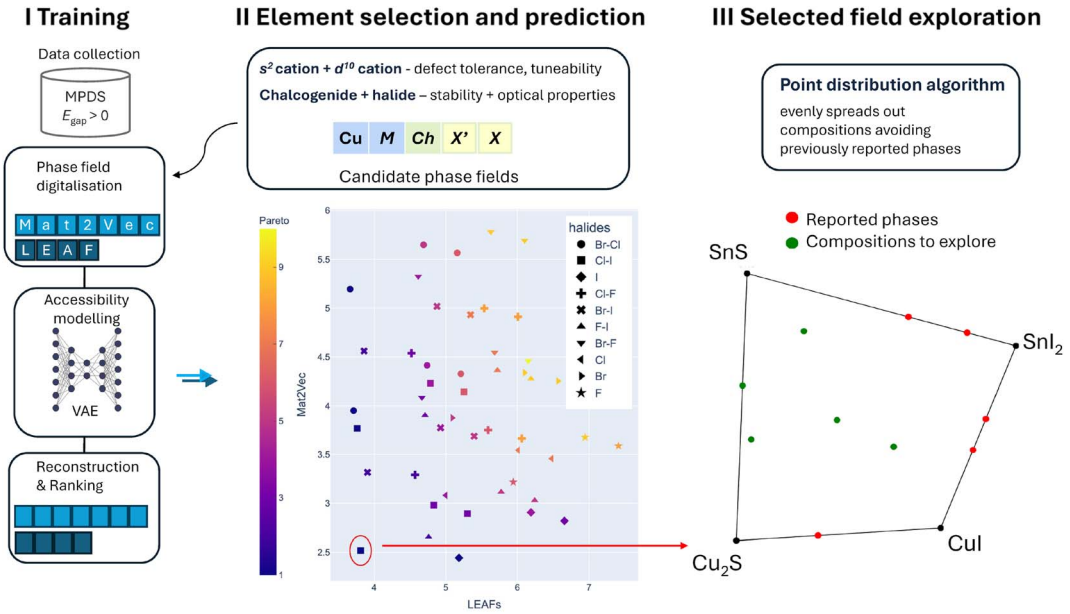

Fig. 1 Phase field and initial composition selection for exploratory synthesis. The VAE models of synthetic accessibility are trained for phase fields for which a band gap value greater than zero is reported in MPDS. Two different models are trained based on Mat2Vec and LEAFs descriptions of constituent elements. At the prediction stage, the Pareto front of the scores from the two models for the candidate combinations of elements is presented, where a lower score denotes higher synthetic accessibility. For the selected highest ranked (lowest score) phase field, a quaternary cut of the Cu–Sn–S–I phase field is explored with the precursors used for the synthesis at the corners. Known ternaries are shown by red points along the boundaries. A points distribution algorithm suggested the five points shown in green as possible starting points, away from known compounds, for exploratory synthesis.

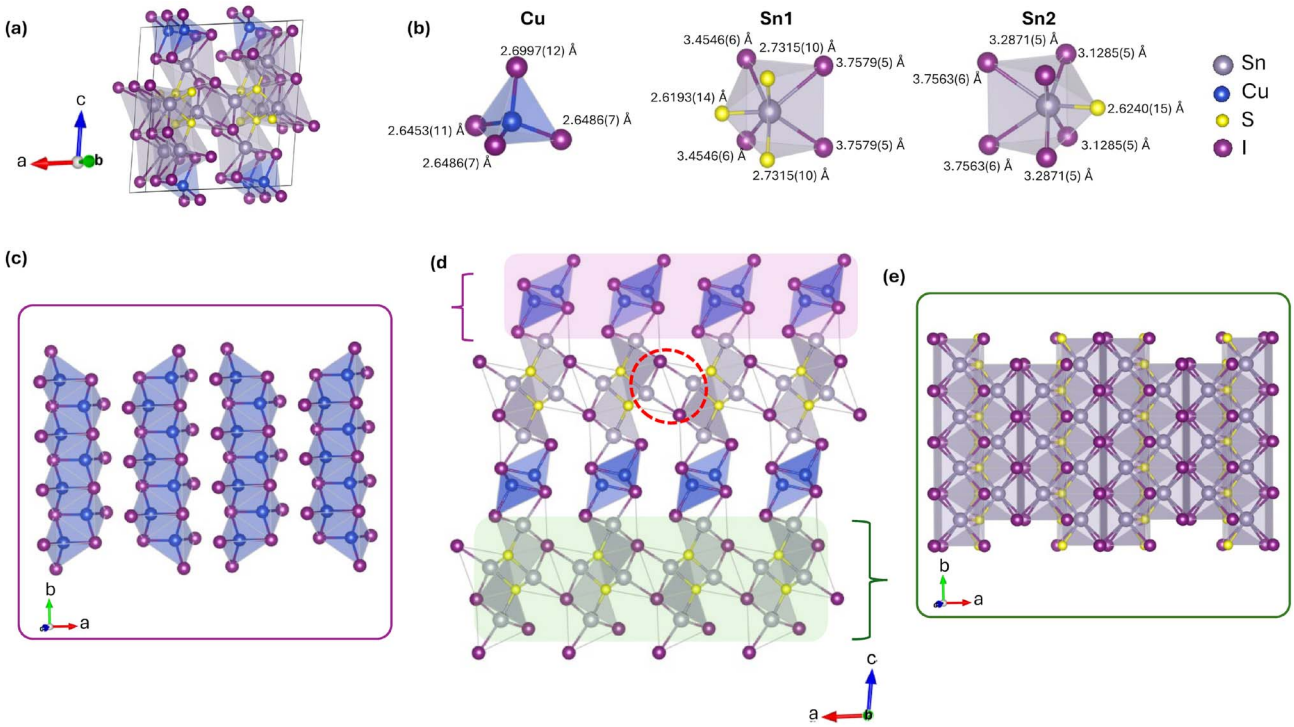

Fig. 2 (a) The three-dimensional crystal structure of $CuSn_2SI_3$. (b) Polyhedral environments for each cation; one CuI_4 tetrahedral site, and the SnS_3I_4 and $SnSI_6$ capped trigonal prismatic environments. (c) CuI_4 tetrahedra share edges along b to form Cu_2I_2 layers. (d) The Cu_2I_2 layers (purple shading) and $Sn_4S_2I_4$ layers (green shading) are stacked along the *c* axis to form the three-dimensional structure of $CuSn_2SI_3$. The red dashed circles highlight longer Sn–I distances (3.7528(8) Å) which provide connectivity along the *a* axis within the $Sn_4S_2I_4$ layer. (e) The Sn polyhedra face share to form $Sn_4S_2I_4$ layers.

cell parameters (obtained from powder XRD) of $a = 14.0369(1)$ Å, $b = 4.30723(5)$ Å, $c = 14.4467(1)$ Å, $\alpha = 90°$ $\beta = 97.007(5)°$, and $\gamma = 90°$ (Tables S11–S17). The structure is formed of three different cation environments (Fig. 2(b)): a slightly distorted tetrahedral copper environment and two different capped trigonal prismatic coordination environments with tin at the centre. The Sn1 site occupies an SnS_3I_4 environment in which the Sn^{2+} cation is displaced from the centre yielding two shorter (3.4546 Å) and two longer (3.7579 Å) Sn–I distances. Sn2 occupies an $SnSI_6$ environment in which the S^{2-} anion caps a single face with a range of Sn–I distances of 3.1285–3.7563 Å, again reflecting the off-centre Sn^{2+} cation position.

These environments combine in $CuSn_2SI_3$ to produce $Sn_4S_2I_4$ layers and Cu_2I_2-like layers which stack alternately along the c axis to give the three-dimensional structure (Fig. 2(d)). Fig. 2(c–e) show the top-down view of both layers. The $Sn_4S_2I_4$ units, formed *via* face-sharing of the SnS_3I_4 and $SnSI_6$ environments (Fig. 2(e)), are connected along the a axis of $CuSn_2SI_3$ by Sn–I distances of 3.7528(8) Å (red dotted circle in Fig. 2(d)), slightly longer than the typical ~3.6 Å Sn–I distances in SnI_2,[51] or Sn_2SI_2.[52] These distances contribute sufficient valence in bond valence sum[53,54] (BVS) calculations, increasing the valence for both the Sn1 and Sn2 sites closer to the formal +2 oxidation state expected for Sn (Table S2–S4). These $Sn_4S_2I_4$ structural units are the same as found in Sn_2SI_2.[52] and Sn_4SI_6,[55] and similar motifs are observed in other chalco–halide compounds such as $Pb_5S_2I_6$.[56] The presence of stereo chemically active lone pair cations can favour the formation of lower dimensional or layered structures, as observed in other s^2 compounds.[29]

The crystal structure of $Cu_{0.35}Sn_{5.29}S_2I_7$ (Fig. 3) was, like $CuSn_2SI_3$, solved from single crystal XRD in the monoclinic space group $C2/m$ with unit cell parameters (at 100 K) of $a = 14.1572(8)$ Å, $b = 4.3847(2)$ Å, $c = 17.1829(11)$ Å, $\alpha = 90°$ $\beta = 110.303(7)°$, and $\gamma = 90°$ (Table S18–S20). The structure consists of the same $Sn_4S_2I_4$ infinite layers as seen in $CuSn_2SI_3$ (Fig. 3(f and g)), thus the in-layer a and b unit cell parameters are comparable between the two materials. These $Sn_4S_2I_4$ layers stack alternately along the c axis with thicker $Cu_{0.35}Sn_{1.29}I_3$ layers (purple layer in Fig. 3(f)) to give the material composition $Cu_{0.35}Sn_{5.29}S_2I_7$, which accounts for the increased c lattice parameter. This thicker $Cu_{0.35}Sn_{1.29}I_3$ layer is disordered (Fig. 3 (c–e)), with partial occupancy of two slightly distorted tetrahedral copper environments (Cu1 occupancy 0.096(4); Cu2 occupancy 0.078(4)) and one octahedral SnI_6 environment (occupancy of 0.644(2)) (Fig. 3(b)) in which the Sn^{2+} cation is displaced from the centre yielding one shorter (3.0567 Å), four similar (~3.099 Å), and one longer (3.2032 Å) Sn–I distances. It is the occupancy of the Sn octahedral site that prevents the complete filling of the neighbouring face-shared Cu tetrahedral sites as seen in ordered $CuSn_2SI_3$, driving the disorder within this layer. The Sn2 site in $Cu_{0.35}Sn_{5.29}S_2I_7$ occupies a similar $SnSI_6$ environment as in $CuSn_2SI_3$, however, the Sn1 site occupies a bicapped trigonal prismatic SnS_3I_5 environment involving one extra I^- compared to $CuSn_2SI_3$ because of a smaller S–Sn–I angle (Fig. 3(g)).

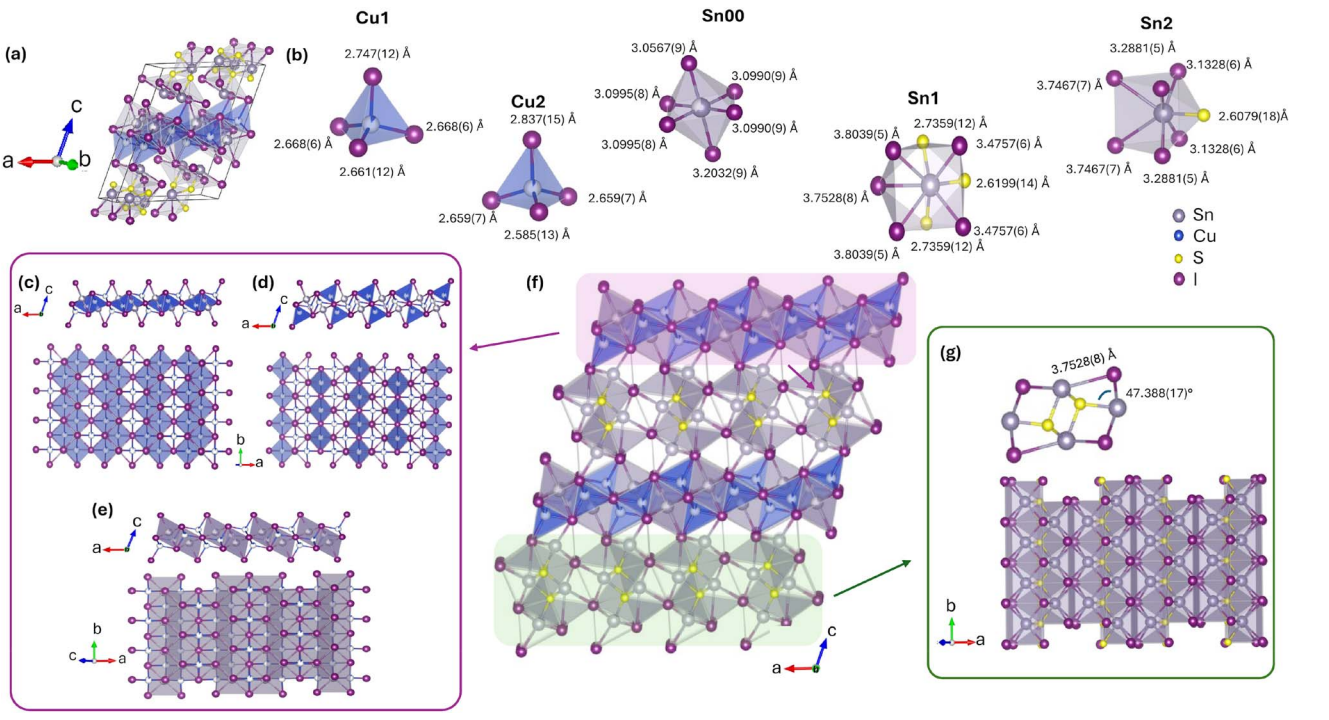

Fig. 3 (a) The three-dimensional crystal structure of $Cu_{0.35}Sn_{5.29}S_2I_7$. (b) Polyhedral environments for each cation; two CuI_4 tetrahedra, a SnI_6 octahedron, a $SnSI_6$ capped trigonal prism, and a SnS_3I_5 bicapped trigonal prism. (c–e) show the arrangement of the tetrahedral Cu and octahedral Sn sites to form the $Cu_{0.35}Sn_{1.29}I_3$ layer. (f) The layered structure of $Cu_{0.35}Sn_{5.2}S_2I_7$, comprising $Cu_{0.35}Sn_{1.29}I_3$ layers (purple shading) and $Sn_4S_2I_4$ layers (green shading). (g) The $Sn_4S_2I_4$ layers are similar to those in ordered $CuSn_2SI_3$ (Fig. 2) with reduced S–Sn–I angles in the $Sn_4S_2I_4$ unit which changes the environment of Sn1 to a bicapped trigonal prism.

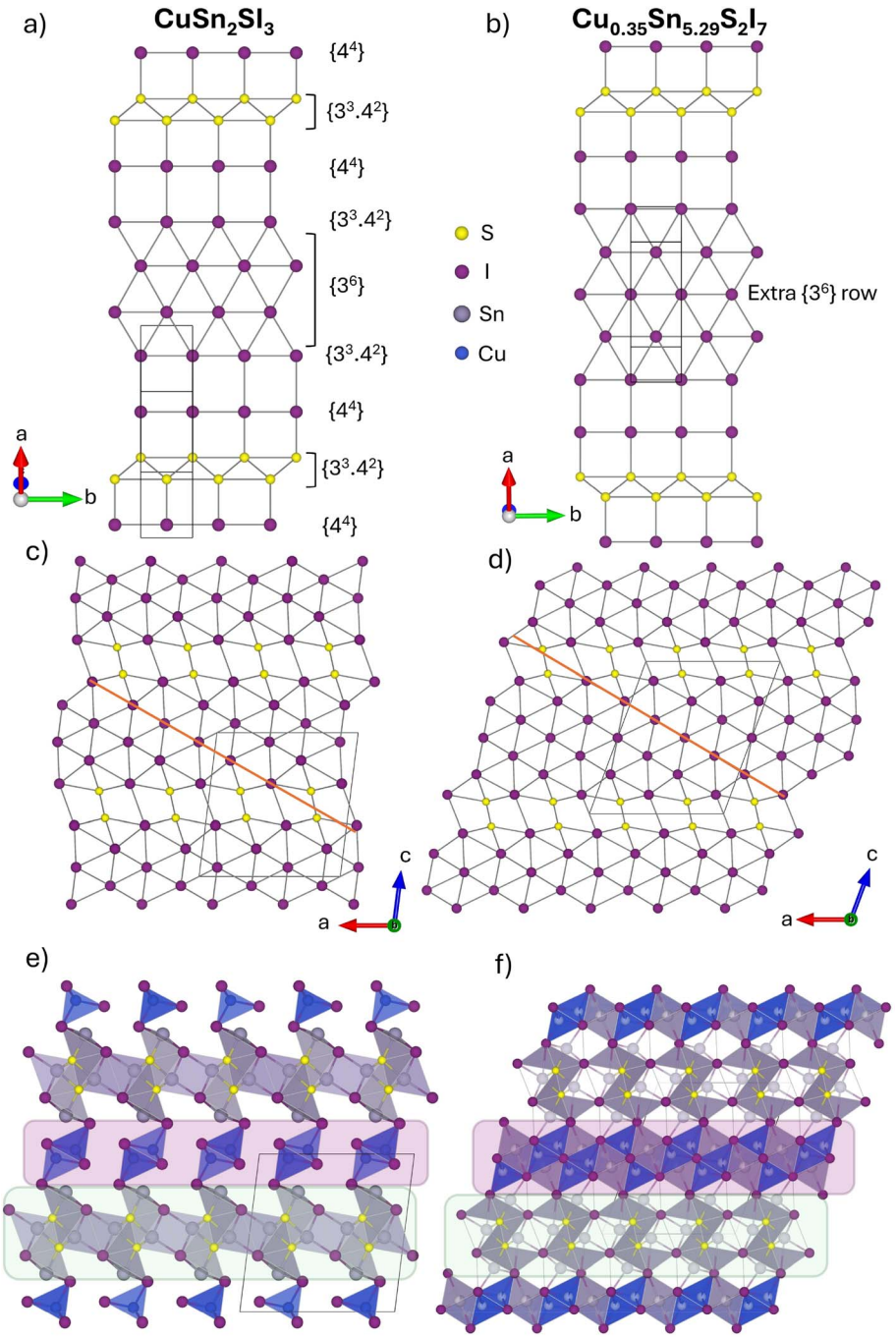

Fig. 4 Comparison of the anion nets in (a) $CuSn_2SI_3$ and (b) $Cu_{0.35}Sn_{5.29}S_2I_7$ with anion rows labelled based on Schäfli notation. The stacking of these nets in (c) and (d) yields layered motifs in the ab plane of S_2I_4 and I^- anions which alternate along the *c* axis. The orange line shown in both (c) and (d) represents the single-layer anion nets shown in (a) and (b). The structures of (e) $CuSn_2SI_3$ and (f) $Cu_{0.35}Sn_{5.29}S_2I_7$ shown along the same projection as in (c) and (d) formed from $Sn_4S_2I_4$ (shaded green) and Cu_2I_2-like (shaded purple) layers.

Similar modifications of the $M_4S_2X_4$ structural motif are observed in $Pb_2BiS_2I_3$ and $Sn_2BiS_2I_3$,[57] while disordered and mobile Cu^+ cations are also a common feature among many Cu-based chalco–halides such as $Cu_3Bi_3S_5I_2$,[58] $Cu_3Bi_2S_3I_3$,[59] and Cu_4BiSeI_4.[60]

The structures of $CuSn_2SI_3$ and $Cu_{0.35}Sn_{5.29}S_2I_7$, with *C*2/*m* symmetry and comparable *a* and *b* lattice parameters, consist of motifs which are common to both materials, such as the $Sn_4S_2I_4$ infinite layers. This can be understood *via* comparison of their anion arrangements (Fig. 4) which are related between the two materials. The anion nets of both $CuSn_2SI_3$ and $Cu_{0.35}Sn_{5.29}S_2I_7$ combine alternating regions of well-known hexagonal and square nets ($\{3^6\}$ and $\{4^4\}$ in Schläfli notation, respectively), separated by five-coordinate S^{2-} anions ($\{3^3.4^2\}$) as shown in Fig. 4(a) and (b). There is one additional row of I^- anions in $Cu_{0.35}Sn_{5.29}S_2I_7$ compared to $CuSn_2SI_3$ (Fig. 4(b)), consistent

with the increased I^- to S^{2-} ratio in $Cu_{0.35}Sn_{5.29}S_2I_7$. These nets stack in similar ways in both structures such that the extended layered motifs become visible within the *ab* plane and alternate along the *c* axes of both structures (Fig. 4(c) and (d)). The additional row of I^- anions in $Cu_{0.35}Sn_{5.29}S_2I_7$ (Fig. 4(b)) expands the *c* lattice parameter compared to $CuSn_2SI_3$. The environments generated by the S_2I_4 layers are occupied exclusively by Sn^{2+} in both materials to yield the $Sn_4S_2I_4$ infinite layers in the *ab* plane (green shading in Fig. 4(e) and (f)). Cu^+ occupies environments within the I^- only layers in both materials (purple shading in Fig. 4(e) and (f)).

The $Sn_4S_2I_4$ unit which exists in both $CuSn_2SI_3$ and $Cu_{0.35}Sn_{5.29}S_2I_7$ is the building block of the ternary Sn_2SI_2 itself and exists in other ternaries such as Sn_4SI_6, and also analogous $M_4S_2X_4$ units (where X = halogen, M = Pb^{2+}, Bi^{3+}, Sb^{3+}) exist in $Pb_5S_2I_6$,[56] BiSI,[61] SbSI,[62] and $CdBiS_2Cl$.[29] The capped trigonal prismatic coordination of cations is common to many of these compounds showcasing the robust nature of these structural units. However, in the case of most other known structures, the addition of a different cation (*i.e.* M-M′-X-X′) leads to it being incorporated into the structural unit either expanding or disrupting the motif, as in cases of $CdBiS_2Cl$, $Cu_3Bi_2S_3I_3$,[59] In_2BiSe_4I,[63] and $Hg_2PbS_2I_2$ [27] (Fig. S2 and Table S5). However, in the case of $CuSn_2SI_3$ and $Cu_{0.35}Sn_{5.29}S_2I_7$, Cu^+ is not incorporated into the $Sn_4S_2I_4$ units and leads to the formation of separate structural layers. The two new compounds discovered here represent some of the few sulphide-iodide quaternary compounds with group 14 s^2 cation (Sn^{2+} or Pb^{2+}). The absence of a large number of similar compounds could be attributed to the large size difference between the S^{2-} and I^- anions.

A $CuSn_2SI_3$ powder sample was prepared by solid state synthesis as described in the Methods. A Rietveld refinement against synchrotron powder X-ray diffraction data is shown in Fig. 5. It confirms the majority phase formed (with 86% weight percent) is the desired $CuSn_2SI_3$, with the primary impurity being $Cu_{0.35}Sn_{5.29}S_2I_7$. Repeated firings and different temperatures did not increase the purity of the samples. The structural and refinement parameters are given in the SI Tables S14 and S15. Powder XRD data measured at 100 K is also shown in the SI (Fig. S3).

The elemental analysis of the crystals and powder sample were carried out using Energy Dispersive X-ray Spectroscopy in a scanning electron microscope. The resulting atomic percentages of Cu, Sn, S, and I are plotted in ternary diagrams in Fig. S4 in SI, along with an image of the crystal in Fig. S5. The measured compositions form a cluster of points close to the target composition. The oxidation states of the various elements present in the $CuSn_2SI_3$ sample were confirmed using the core level XPS measurements, and are shown in SI Fig. S6–S10. The binding energies obtained from fitting the spectra were compared with the values from the literature to confirm the oxidation states of the different species present in the compound (Tables S6–S9). The values obtained agree with the assignment of the oxidation states Cu^+, Sn^{2+}, S^{2-}, and I^- in $CuSn_2SI_3$.

Optical property measurements

To gain an understanding of the optical properties and band gap of the material, UV-visible spectroscopy was carried out on the powder sample of $CuSn_2SI_3$. The measured diffuse reflectance

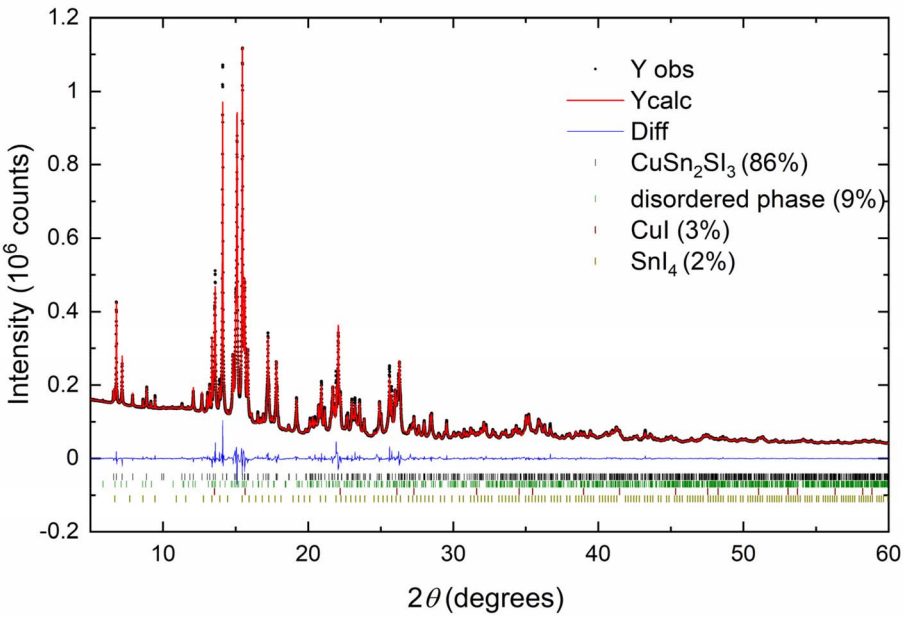

Fig. 5 Synchrotron powder X-ray diffraction pattern of as synthesised $CuSn_2SI_3$ sample measured at room temperature. $CuSn_2SI_3$ constitutes 86% by weight of the sample, with the disordered $Cu_{0.35}Sn_{5.29}S_2I_7$ being the primary impurity and the binary iodides present in small amounts. Black circles show the measured data and the red line is the calculated pattern from a Rietveld refinement. The difference between the two are shown as a blue line and the Bragg peak positions of the phases present are plotted as well.

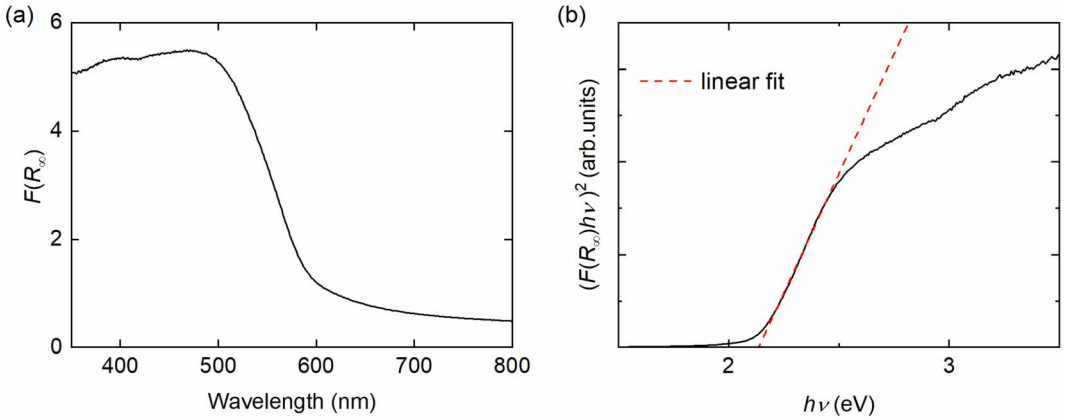

Fig. 6 The pseudo-absorption spectrum for $CuSn_2SI_3$ measured using UV-Vis spectroscopy. (a) The measured diffuse reflectance data is plotted after transforming as Kubelka–Munk function $F(R_\infty)$ as a function of wavelength. (b) A Tauc plot for the absorption spectra assuming a direct band gap. Red dotted line shows the linear fit giving a band gap of $E_g = 2.1 \pm 0.2$ eV.

data was converted using the Kubelka–Munk function[64,65] and plotted in Fig. 6. The absorption falls sharply above ~500 nm, indicating an absorption onset around that energy range, consistent with the orange-red colour of the sample. To estimate the optical band gap, a Tauc analysis[66] was performed assuming a direct band gap, as shown in Fig. 6(b). The linear fit to the plot of $(F(R_\infty)h\nu)^2$ *versus* $h\nu$ gives an intercept to the *x*-axis, at 2.1 ± 0.2 eV (error defined as the standard deviation obtained from multiple measurements from the same batch of powder sample). However, the powder sample is not phase pure and the impurities present could be contributing to the absorption edge and hence the band gap values obtained this way. We eliminate the possibility that the absorption onset is coming from either CuI or SnI_4, as CuI has a much wider gap of ~3 eV[67,68] and by measuring samples with added SnI_4 to examine the effect this has on the absorption spectra (Fig. S11). Although SnI_4 has a bandgap close to where we see the absorption edge, we conclude ~2% of SnI_4 cannot give rise to the absorbance we observe from the powder sample of $CuSn_2SI_3$. This leaves the determined band gap to be from a mixture of $CuSn_2SI_3$ and $Cu_{0.35}Sn_{5.29}S_2I_7$. Although the measured optical absorption onset suggests a band gap of approximately 2.1 eV, which is too high for use in a single junction solar cell, one cannot rule out the potential for use in a multijunction cell, for example in conjunction with perovskites, where absorption occurs across the visible energy ranges and record high efficiencies are reported.[69] Also, it is to be noted that this is the first report in the Cu–Sn chalco–halide family of compounds. Further exploration and attempts to tune the band

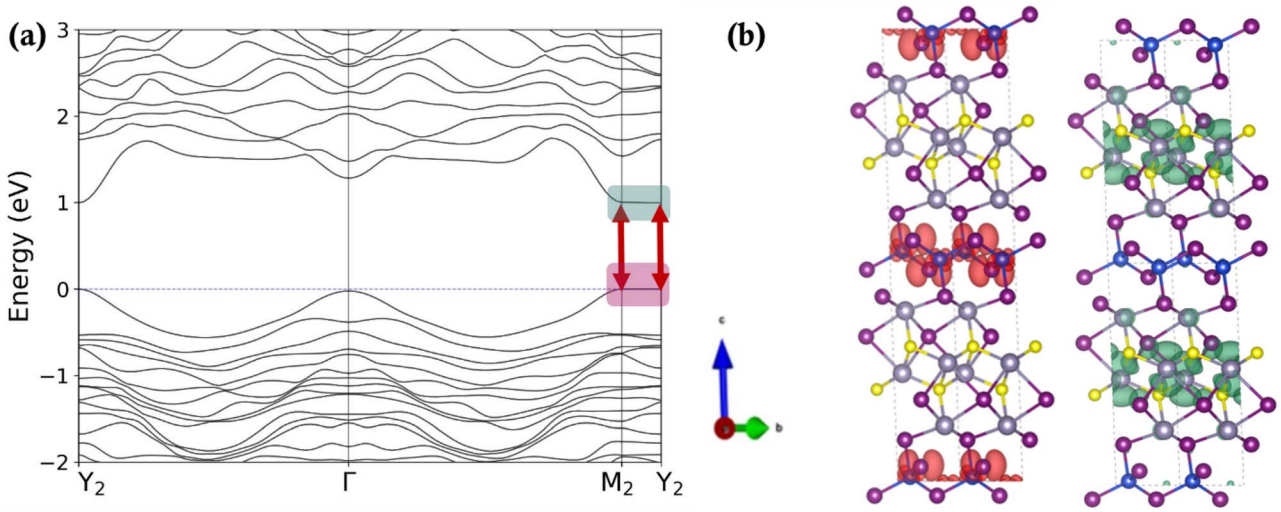

Fig. 7 . (a) The electronic band structure calculated for the ordered phase of the relaxed structure of $CuSn_2SI_3$ using DFT(PBE) + SOC along the closed path Y_2–Γ–M_2–Y_2 in the Brillouin zone (See SI Fig. S12(a) and S12(b) for the band structure along the full path for the experimental as well as the relaxed structure, respectively, with the Brillouin zone shown in Fig. S12(c)). The orbital projected k-resolved DOS in the Brillouin zone and the partial DOS for each atom is shown in SI Fig. S13. 7(b) The charge density distribution corresponding to the valence band top (VBT) (red shaded regions) and the conduction band bottom (CBB) (green shared regions) at the point Y_2 in reciprocal space that also corresponds to the direct bandgap.

gap by examining analogues and by chemical substitution are possible avenues for future research.

Electronic band structure calculations

The electronic band structure of $CuSn_2SI_3$, shown in Fig. 7(a), is calculated from DFT (PBE) + SOC along a path Y_2 (−0.5, 0.5, 0) – Γ (0, 0, 0) – M_2 (−0.5, 0.5, 0.5) – Y_2 in reciprocal lattice units. See Fig. S12(a) and S12(b) for the full path. We find a direct band gap, with dispersive bands in the directions corresponding to the Cu–I or Sn–S–I planes of the structure, and non-dispersive otherwise (for example along Y_2–M_2). As shown in Table 1, we calculate a band gap of ∼1.0 eV within semi-local DFT (PBE) + SOC, and of ∼2.5 and ∼1.8 eV using the PBE0 [70] and the HSE[71] hybrid functionals, respectively. The differences between these calculated band gaps and the experimental band gap estimated from optical absorption experiments are consistent with previous benchmarking data reported in the literature.[72]

To better understand the origin of flat bands between Y_2 and M_2, we computed the charge density distribution for the valence band top (VBT) and the conduction band bottom (CBB) at these specific points in the Brillouin zone (see Fig. 7(b) for Y_2). The red and green iso-surfaces show the charge density at the VBT and the CBB, respectively. The charge density corresponding to the VBT is clearly centred around the Cu_2I_2 layers. Along the crystallographic *c*-axis, each such layer is spatially well separated from the next one by the $Sn_4S_2I_4$ layer in between leading to minimal overlap between the different Cu_2I_2 layers. This leads to the formation of a flat band at the VBT along the corresponding direction in *k*-space which is Y_2–M_2. Similarly, the charge surfaces for the CBB are primarily centred around the Sn atoms in the $Sn_4S_2I_4$ layers and separated along the *c*-axis, leading to a flat band at the CBB as well. Further, the atom-projected band structure shown in SI Fig. S13 with corresponding atom and orbital resolved density of states (DOS) confirms that the contributions to the VBT arise primarily from Cu and I atomic orbitals, while the CBB consists mostly of Sn with very small contributions from S and I orbitals. The presence of flat bands along with dispersive bands in the Y_2–Γ–M_2 direction indicates a possibility of highly anisotropic electron and hole transport. To quantify this, we calculated and compared the effective masses of the holes and electrons at the high symmetry points Y_2 and M_2 along the three directions, as tabulated in Table 2.

The effective mass calculations at Y_2 and M_2 show clear anisotropy in three different directions. The direction along the crystallographic *c*-axis (m_3) has the heaviest effective masses for both holes and electrons. In the other two orthogonal directions the effective masses are much smaller at a fraction of a free electron mass indicating a possible high mobility of charge carriers. Also, the average effective mass of the holes is ∼3 times larger than the average effective mass of the electrons. It is to be noted that, in semiconductors with anisotropic and non-parabolic bands, the experimental effective mass often depends on the carrier concentration[73,74] which we are not considering in our calculations here. Despite highly anisotropic chemical and electronic structures many materials like Sb_2Se_3,[75] BiSI,[76] *etc.* have been successfully incorporated into solar cells with high efficiency with careful synthesis of oriented thin films. Thus, the anisotropic electronic bands do not rule out the potential of $CuSn_2SI_3$ for solar absorber applications.

An understanding of the contributions to the band edges coming from different elements is critical to further understand the photo-induced charge carrier transport and to predict ways to tune the band gap. We compare the DOS near the Fermi energy obtained from DFT calculations with an experimentally measured X-ray photoemission spectroscopy valence band spectrum for $CuSn_2SI_3$ in Fig. 8. The calculated density of states has been processed with a Gaussian smearing of 0.25 eV accounting for the lifetime broadening in the measured data and spectrometer resolution,[77,78] to aid comparison with the experimental data. The background was subtracted from the measured XPS data and scaled to match with the DOS.

The total DOS and the XPS valence band data agree reasonably well. As discussed before, the VBT contributions come primarily from Cu and some overlap with I, according to DFT calculations. The measured XPS spectrum shows a broad and asymmetric peak, centered around ∼2.5 eV. The calculations roughly capture this peak position, with the asymmetric peak

Table 1 Comparison of the experimentally obtained bandgap with predictions from DFT + SOC and DFT + SOC with Hybrid functionals PBE0 and HSE, for the volume relaxed structure of $CuSn_2SI_3$

Method	Bandgap (eV)
Experiment	2.1 ± 0.2
DFT	1.0
PBE0	2.45
HSE	1.79

Table 2 Effective masses at the valence band top and the conduction band bottom for the high symmetry *k*-points M_2 and Y_2 for $CuSn_2SI_3$ in units of electron mass (m_e) along the specified direction of eigenvectors in crystal units in the reciprocal space

High-symmetry point	m^* (m_e) (Harmonic mean)	$m_1(m_e)$ (direction)	m_2 (m_e) (direction)	m_3 (m_e) (direction)
M_2 (−0.5, 0.5, 0.5)	VBT (hole) 1.31	0.45 (1, −1, 0)	>>1 (1, 1, 0.09)<	>> 1 (0.04, 0.04, 1)
	CBB (electron) 0.45	0.21 (1, −1, 0)	0.56 (1, 1, −0.04)	>>1 (0.16, 0.16, 1)
Y_2 (−0.5, 0.5, 0)	VBT (hole) 1.40	0.48 (−1, 1, 0)	>>1 (1, 1, −0.21)	>>1 (0.32, 0.32, 1)
	CBB (electron) 0.46	0.21(1, −1, 0)	0.59 (1, 1, 0.03)	>>1 (0.1, 0.1, 1)
Γ(0, 0, 0)	VBT (hole) 2.58	0.92 (1, −1, 0)	>>1 (1, 1, −0.07)	>> 1 (0.19, 0.19, 1)
	CBB (electron) 0.72	0.423 (1, −1, 0)	1.9 (1, 1, 0.91)	0.78 (−0.85, −0.85, 1)

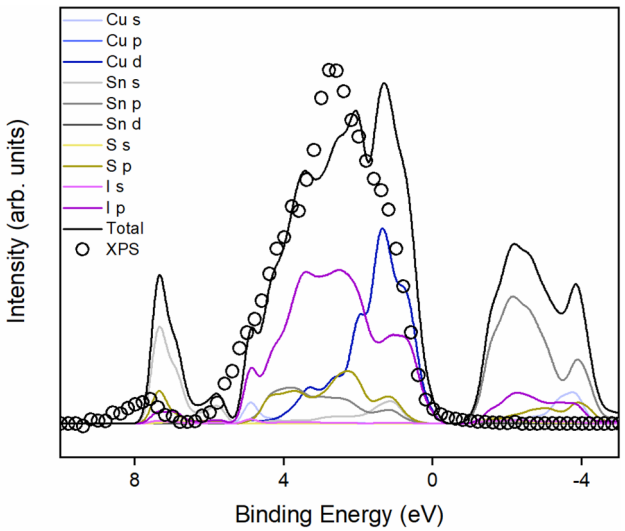

Fig. 8 Comparison of the total density of states as obtained from DFT + SOC and the valence band spectrum obtained from X-ray photoemission spectroscopy measurements. The DFT data has an experimentally motivated Gaussian smearing of 0.25 eV.

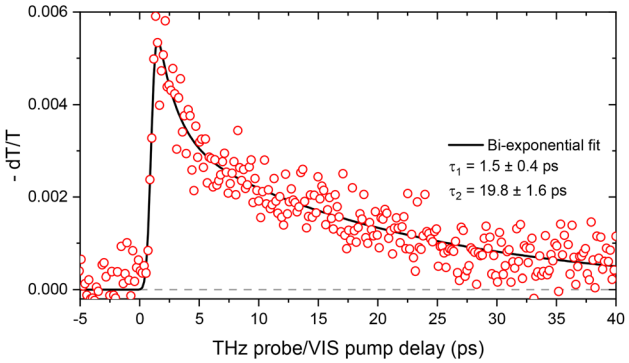

Fig. 9 Differential transmission of the THz electric field amplitude, proportional to THz transient photoconductivity, recorded using optical-pump terahertz-probe spectroscopy for a $CuSn_2SI_3$ cold-pressed pellet. Curves were recorded following excitation with 400 nm (3.1 eV) light pulses of 200 mJ cm^{-2} fluence. A value of $\varphi\mu$ = 1.3 ± 0.2 cm^2 V^{-1} s^{-1} was extracted for the effective electron–hole sum mobility from the peak value after excitation under knowledge of the density of absorbed photons.

centered around ~2 eV with multiple shoulders. The smaller peak further away from the Fermi energy (~7.5 eV) is also reproduced, although with a much higher intensity and with a slight shift. The disparities in intensity could be arising, in part, from the different photoionization cross sections for different atomic orbitals, which are not accounted for in DOS calculations. We also note that the relative intensity of the main peak and the peak at ~1 eV in calculations (which is a barely visible shoulder in experimental data) is better reproduced with PBE0 and HSE DOS, as shown in SI Fig. S14. This is expected, as the semi-local DFT not only underestimates the band gap, but also band widths.[72] Nevertheless, the general agreement between DFT and XPS data shows that the calculations have captured the band edge properties of the compound very well.

Charge carrier mobility

Terahertz (THz) photoconductivity measurements were performed to assess the mobility and dynamics of charge carriers in $CuSn_2SI_3$. Fig. 9 shows the change in photoconductivity in a cold-pressed pellet of $CuSn_2SI_3$ as a function of time after photoexcitation with 35 fs-laser pulses at a photon energy of 3.1 eV. From the value of the initial amplitude immediately after excitation, and under knowledge of the absorbed photon density (see SI for details) a value of the effective electron–hole sum mobility of $\varphi\mu = 1.3 \pm 0.2$ cm^2 (V s^{-1}) was extracted. This value is comparable to THz mobilities measured for other newly emerging solar absorbers, such as $Cu_{4x}(AgBi)_{1-x}I_4$,[79] $(AgI)_x(BiI_3)_y$ rudorffites[80] and $AgBiS_2$,[81] but about an order of magnitude lower than those typical for tin iodide perovskites.[82] The conductivity signal decays within the first ~10 ps after photoexcitation, suggesting rapid recombination or trapping of charge carriers, which may be mediated by both point defects and impurity phases. Since both types of defects may also influence the charge-carrier mobility through scattering events, further material purification and refinement is likely to offer increases in both mobility and lifetime of charge carriers.

Conclusions

We discover two new semiconducting Cu-containing chalco–halides, $CuSn_2SI_3$ and $Cu_{0.35}Sn_{5.29}S_2I_7$, through exploratory synthesis guided by computational tools. These compounds form a three-dimensional structure with related anion lattices. Layers of $Sn_4S_2I_4$ are connected by different layers forming the two different compounds, highlighting the structural versatility and possibility to explore more such structures. $CuSn_2SI_3$ has a band gap in the visible region of ~2 eV and moderate charge-carrier mobilities comparable to those of recently emerging new solar absorber materials in the metal halide and chalcogenide space, making this a possible candidate material for solar absorber applications, *e.g.*, in multi-junction cells with further design and further tuning of the bandgap. Electronic band structure calculations using DFT suggest $CuSn_2SI_3$ to be a direct band gap material with flat bands formed due to lack of overlap between the Cu_2I_2 and $Sn_4S_2I_4$ layers, and highly anisotropic effective masses. These compounds open a relatively less explored class of d^{10}–s^2 cations containing chalco–halides as a path for making semiconductors with promising electronic properties.

Author contributions

B. K., T. D. M., and M. J. R. developed the project direction. B. K. discovered and synthesized the materials. L. M. D., T. D. M., and J. B. C. advised on the synthesis. B. K., J. P. S., C. M. R., J. B. C., and L. M. D. characterized the crystal structure. D. B. carried out DFT calculations under the supervision of M. R. F. A. V. developed ML models. D. R. developed the points distribution algorithm under the supervision of M. S. D. UV-vis measurements

were done by B. K. under the supervision of T. D. M. D. M. and L. H. performed Terahertz spectroscopy measurements and analysis. M. Z. performed SEM-EDX measurements and analysed the data. C. J. H. did X. P. S. measurements and advised on analysis. B. K. developed the initial draft with inputs from D. B., A. V., and D. M. All authors were involved in discussions and evaluations of the drafts during the writing process. M. J. R. directed the project and acquired funding.

Conflicts of interest

There are no conflicts to declare.

Data availability

CCDC 2503028 and 2503027 contain the supplementary crystallographic data for this paper.[83a,b]

The data that support the findings of this research are openly available on the University of Liverpool Data Repository (https://doi.org/10.17638/datacat.liverpool.ac.uk/3072).

Supplementary information (SI): literature information; Structure comparison of $CuSn_2SI_3$ and $Cu_{0.35}Sn_{5.29}S_2I_7$; Synchrotron PXRD; Elemental analysis; Sample images; XPS data; UV-visible spectroscopy; electronic band structures; Terahertz spectroscopy; crystallographic data. See DOI: https://doi.org/10.1039/d5ta06204g.

Acknowledgements

We thank Dr. Krzystof Pawlak (Materials Innovation Factory, University of Liverpool) for assistance with UV-Vis measurements. We acknowledge funding from the Engineering and Physical Sciences Research Council (EPSRC) under EP/X038777/1 and EP/V026887. The Leverhulme Trust *via* the Leverhulme Research Centre for Functional Materials Design is thanked for support of J.P.S. This work was possible due to use of the shared analytical equipment of the Materials Innovation Factory (created as part of the UK Research Partnership Innovation Fund (Research England) and co-funded by the Sir Henry Royce Institute). X-ray photoelectron (XPS) data were acquired at the EPSRC National Facility for XPS ("HarwellXPS", EP/Y023587/1, EP/Y023609/1, EP/Y023536/1, EP/Y023552/1 and EP/Y023544/1). We thank Diamond Light Source for access to beamline I-11 (CY37989). M.R.F and D.B acknowledge computational resources provided by the Texas Advanced Computing Center (TACC) at UT Austin using the Frontera system through the Frontera Pathways allocation DMR23008.

References

1 M. A. Green, A. Ho-Baillie and H. J. Snaith, The emergence of perovskite solar cells, *Nat. Photonics*, 2014, **8**, 506–514.
2 N.-G. Park, Perovskite solar cells: an emerging photovoltaic technology, *Mater. Today*, 2015, **18**, 65–72.
3 H. J. Snaith, Present status and future prospects of perovskite photovoltaics, *Nat. Mater.*, 2018, **17**, 372–376.
4 A. K. Jena, A. Kulkarni and T. Miyasaka, Halide Perovskite Photovoltaics: Background, Status, and Future Prospects, *Chem. Rev.*, 2019, **119**, 3036–3103.
5 M. M. Lee, J. Teuscher, T. Miyasaka, T. N. Murakami and H. J. Snaith, Efficient Hybrid Solar Cells Based on Meso-Superstructured Organometal Halide Perovskites, *Science*, 2012, **338**, 643–647.
6 H. Min, D. Y. Lee, J. Kim, G. Kim, K. S. Lee, J. Kim, M. J. Paik, Y. K. Kim, K. S. Kim, M. G. Kim, T. J. Shin and S. Il Seok, Perovskite solar cells with atomically coherent interlayers on SnO_2 electrodes, *Nature*, 2021, **598**, 444–450.
7 Z. Li, T. R. Klein, D. H. Kim, M. Yang, J. J. Berry, M. F. A. M. van Hest and K. Zhu, Scalable fabrication of perovskite solar cells, *Nat. Rev. Mater.*, 2018, **3**, 1–20.
8 Z. Xiao, Z. Song and Y. Yan, From Lead Halide Perovskites to Lead-Free Metal Halide Perovskites and Perovskite Derivatives, *Adv. Mater.*, 2019, **31**, 1803792.
9 J. Zhuang, J. Wang and F. Yan, Review on Chemical Stability of Lead Halide Perovskite Solar Cells, *Nano-Micro Lett.*, 2023, **15**, 84.
10 F. De Angelis, The Prospect of Lead-Free Perovskite Photovoltaics, *ACS Energy Lett.*, 2021, **6**, 1586–1587.
11 R. E. Brandt, J. R. Poindexter, P. Gorai, R. C. Kurchin, R. L. Z. Hoye, L. Nienhaus, M. W. B. Wilson, J. A. Polizzotti, R. Sereika, R. Žaltauskas, L. C. Lee, J. L. MacManus-Driscoll, M. Bawendi, V. Stevanović and T. Buonassisi, Searching for "Defect-Tolerant" Photovoltaic Materials: Combined Theoretical and Experimental Screening, *Chem. Mater.*, 2017, **29**, 4667–4674.
12 A. M. Ganose, C. N. Savory and D. O. Scanlon, Beyond methylammonium lead iodide: prospects for the emergent field of ns^2 containing solar absorbers, *Chem. Commun.*, 2017, **53**, 20–44.
13 H. Kageyama, K. Hayashi, K. Maeda, J. P. Attfield, Z. Hiroi, J. M. Rondinelli and K. R. Poeppelmeier, Expanding frontiers in materials chemistry and physics with multiple anions, *Nat. Commun.*, 2018, **9**, 772.
14 U. V. Ghorpade, M. P. Suryawanshi, M. A. Green, T. Wu, X. Hao and K. M. Ryan, Emerging Chalcohalide Materials for Energy Applications, *Chem. Rev.*, 2023, **123**, 327–378.
15 C. Ming, Z. Chen, F. Zhang, S. Gong, X. Wu, J. Jiang, T. Ye, Q. Xu, K. Yang, L. Wang, X. Cao, S. Yang, S. Zhang, Y. Zhang, J. Shi and Y.-Y. Sun, Mixed Chalcogenide-Halides for Stable, Lead-Free and Defect-Tolerant Photovoltaics: Computational Screening and Experimental Validation of $CuBiSCl_2$ with Ideal Band Gap, *Adv. Funct. Mater.*, 2022, **32**, 2112682.
16 J. He, X. Hu, Z. Liu, W. Chen and G. Longo, Prospect for Bismuth/Antimony Chalcohalides-Based Solar Cells, *Adv. Funct. Mater.*, 2023, **33**, 2306075.
17 K. T. Butler, S. McKechnie, P. Azarhoosh, M. van Schilfgaarde, D. O. Scanlon and A. Walsh, Quasi-particle electronic band structure and alignment of the V-VI-VII semiconductors SbSI, SbSBr, and SbSeI for solar cells, *Appl. Phys. Lett.*, 2016, **108**, 112103.

18 A. M. Ganose, S. Matsumoto, J. Buckeridge and D. O. Scanlon, Defect Engineering of Earth-Abundant Solar Absorbers BiSI and BiSeI, *Chem. Mater.*, 2018, **30**, 3827–3835.
19 J. Wang and S. Y. Quek, Isolated flat bands and physics of mixed dimensions in a 2D covalent organic framework, *Nanoscale*, 2020, **12**, 20279–20286.
20 G. Sethi, M. Cuma and F. Liu, Excitonic Condensate in Flat Valence and Conduction Bands of Opposite Chirality, *Phys. Rev. Lett.*, 2023, **130**, 186401.
21 G. Pasquale, Z. Sun, K. Čerņevičs, R. Perea-Causin, F. Tagarelli, K. Watanabe, T. Taniguchi, E. Malic, O. V. Yazyev and A. Kis, Flat-Band-Induced Many-Body Interactions and Exciton Complexes in a Layered Semiconductor, *Nano Lett.*, 2022, **22**, 8883–8891.
22 S. B. Zhang, S.-H. Wei, A. Zunger and H. Katayama-Yoshida, Defect physics of the $CuInSe_2$ chalcopyrite semiconductor, *Phys. Rev. B*, 1998, **57**, 9642–9656.
23 A. Zakutayev, C. M. Caskey, A. N. Fioretti, D. S. Ginley, J. Vidal, V. Stevanovic, E. Tea and S. Lany, Defect Tolerant Semiconductors for Solar Energy Conversion, *J. Phys. Chem. Lett.*, 2014, **5**, 1117–1125.
24 A. Nicolson, S. R. Kavanagh, C. N. Savory, G. W. Watson and D. O. Scanlon, Cu_2SiSe_3 as a promising solar absorber: harnessing cation dissimilarity to avoid killer antisites, *J. Mater. Chem. A*, 2023, **11**, 14833–14839.
25 G. Volonakis, M. R. Filip, A. A. Haghighirad, N. Sakai, B. Wenger, H. J. Snaith and F. Giustino, Lead-Free Halide Double Perovskites via Heterovalent Substitution of Noble Metals, *J. Phys. Chem. Lett.*, 2016, **7**, 1254–1259.
26 M.-Y. Ran, S.-H. Zhou, W. Wei, B.-J. Song, Y.-F. Shi, X.-T. Wu, H. Lin and Q.-L. Zhu, Quaternary Chalcohalides $CdSnSX_2$ (X = Cl or Br) with Neutral Layers: Syntheses, Structures, and Photocatalytic Properties, *Inorg. Chem.*, 2021, **60**, 3431–3438.
27 R. Blachnik, W. Buchmeier and H. A. Dreisbach, Structure of lead(II) dimercury(II) diiodide disulfide, *Acta Crystallogr. C*, 1986, **42**, 515–517.
28 A. Pfitzner, $CuI)_2Cu_3SbS_3$: Copper Iodide as Solid Solvent for Thiometalate ions, *Chem.–Eur. J.*, 1997, **3**, 2032–2038.
29 L. Wang, Y.-C. Hung, S.-J. Hwu, H.-J. Koo and M.-H. Whangbo, Synthesis, Structure, and Properties of a New Family of Mixed-Framework Chalcohalide Semiconductors: $CdSbS_2X$ (X = Cl, Br), $CdBiS_2X$ (X = Cl, Br), and $CdBiSe_2X$ (X = Br, I), *Chem. Mater.*, 2006, **18**, 1219–1225.
30 A. Vasylenko, J. Gamon, B. B. Duff, V. V. Gusev, L. M. Daniels, M. Zanella, J. F. Shin, P. M. Sharp, A. Morscher, R. Chen, A. R. Neale, L. J. Hardwick, J. B. Claridge, F. Blanc, M. W. Gaultois, M. S. Dyer and M. J. Rosseinsky, Element selection for crystalline inorganic solid discovery guided by unsupervised machine learning of experimentally explored chemistry, *Nat. Commun.*, 2021, **12**, 5561.
31 A. Vasylenko, D. Antypov, V. V. Gusev, M. W. Gaultois, M. S. Dyer and M. J. Rosseinsky, Element selection for functional materials discovery by integrated machine learning of elemental contributions to properties, *npj Comput. Mater.*, 2023, **9**, 1–10.
32 A. Blokhin and P. Villars, https://mpds.io.
33 V. Tshitoyan, J. Dagdelen, L. Weston, A. Dunn, Z. Rong, O. Kononova, K. A. Persson, G. Ceder and A. Jain, Unsupervised word embeddings capture latent knowledge from materials science literature, *Nature*, 2019, **571**, 95–98.
34 D. Ritchie, M. W. Gaultois, V. V. Gusev, V. Kurlin, M. J. Rosseinsky and M. S. Dyer, Probabilistic Isolation of Crystalline Inorganic Phases, *J. Chem. Inf. Model.*, 2025, **65**, 13226–13237.
35 G. M. Sheldrick, A short history of SHELX, *Acta Crystallogr. A*, 2008, **64**, 112–122.
36 O. V. Dolomanov, L. J. Bourhis, R. J. Gildea, J. a. K. Howard and H. Puschmann, OLEX2: a complete structure solution, refinement and analysis program, *J. Appl. Crystallogr.*, 2009, **42**, 339–341.
37 K. Momma and F. Izumi, VESTA 3 for three-dimensional visualization of crystal, volumetric and morphology data, *J. Appl. Crystallogr.*, 2011, **44**, 1272–1276.
38 A. A. Coelho, Whole-profile structure solution from powder diffraction data using simulated annealing, *J. Appl. Crystallogr.*, 2000, **33**, 899–908.
39 P. Hohenberg and W. Kohn, Inhomogeneous Electron Gas, *Phys. Rev.*, 1964, **136**, B864–B871.
40 W. Kohn and L. J. Sham, Self-Consistent Equations Including Exchange and Correlation Effects, *Phys. Rev.*, 1965, **140**, A1133–A1138.
41 P. Giannozzi, S. Baroni, N. Bonini, M. Calandra, R. Car, C. Cavazzoni, D. Ceresoli, G. L. Chiarotti, M. Cococcioni, I. Dabo, A. Dal Corso, S. de Gironcoli, S. Fabris, G. Fratesi, R. Gebauer, U. Gerstmann, C. Gougoussis, A. Kokalj, M. Lazzeri, L. Martin-Samos, N. Marzari, F. Mauri, R. Mazzarello, S. Paolini, A. Pasquarello, L. Paulatto, C. Sbraccia, S. Scandolo, G. Sclauzero, A. P. Seitsonen, A. Smogunov, P. Umari and R. M. Wentzcovitch, QUANTUM ESPRESSO: a modular and open-source software project for quantum simulations of materials, *J. Phys. Condens. Matter*, 2009, **21**, 395502.
42 P. Giannozzi, O. Andreussi, T. Brumme, O. Bunau, M. Buongiorno Nardelli, M. Calandra, R. Car, C. Cavazzoni, D. Ceresoli, M. Cococcioni, N. Colonna, I. Carnimeo, A. Dal Corso, S. de Gironcoli, P. Delugas, R. A. DiStasio, A. Ferretti, A. Floris, G. Fratesi, G. Fugallo, R. Gebauer, U. Gerstmann, F. Giustino, T. Gorni, J. Jia, M. Kawamura, H.-Y. Ko, A. Kokalj, E. Küçükbenli, M. Lazzeri, M. Marsili, N. Marzari, F. Mauri, N. L. Nguyen, H.-V. Nguyen, A. Otero-de-la-Roza, L. Paulatto, S. Poncé, D. Rocca, R. Sabatini, B. Santra, M. Schlipf, A. P. Seitsonen, A. Smogunov, I. Timrov, T. Thonhauser, P. Umari, N. Vast, X. Wu and S. Baroni, Advanced capabilities for materials modelling with Quantum ESPRESSO, *J. Phys. Condens. Matter*, 2017, **29**, 465901.
43 J. P. Perdew, K. Burke and M. Ernzerhof, Generalized Gradient Approximation Made Simple, *Phys. Rev. Lett.*, 1996, **77**, 3865–3868.
44 D. R. Hamann, Optimized norm-conserving Vanderbilt pseudopotentials, *Phys. Rev. B*, 2013, **88**, 085117.
45 M. J. van Setten, M. Giantomassi, E. Bousquet, M. J. Verstraete, D. R. Hamann, X. Gonze and

G.-M. Rignanese, The PseudoDojo: Training and grading a 85 element optimized norm-conserving pseudopotential table, *Comput. Phys. Commun.*, 2018, **226**, 39–54.

46 A. Fonari, C. Sutton, Effective Mass Calculator , 2012, https://github.com/afonari/emc.

47 A. Faghaninia, Handy-VASP-DFT-Calculations-Scripts, 2016, https://github.com/albalu/Handy-VASP-DFT-Calculations-Scripts/blob/master/README.md.

48 C. Q. Xia, J. Peng, S. Poncé, J. B. Patel, A. D. Wright, T. W. Crothers, M. Uller Rothmann, J. Borchert, R. L. Milot, H. Kraus, Q. Lin, F. Giustino, L. M. Herz and M. B. Johnston, Limits to Electrical Mobility in Lead-Halide Perovskite Semiconductors, *J. Phys. Chem. Lett.*, 2021, **12**, 3607–3617.

49 M. Righetto, S. Caicedo-Dávila, M. T. Sirtl, V. J.-Y. Lim, J. B. Patel, D. A. Egger, T. Bein and L. M. Herz, Alloying Effects on Charge-Carrier Transport in Silver–Bismuth Double Perovskites, *J. Phys. Chem. Lett.*, 2023, **14**, 10340–10347.

50 C. L. Davies, J. Borchert, C. Q. Xia, R. L. Milot, H. Kraus, M. B. Johnston and L. M. Herz, Impact of the Organic Cation on the Optoelectronic Properties of Formamidinium Lead Triiodide, *J. Phys. Chem. Lett.*, 2018, **9**, 4502–4511.

51 R. A. Howie, W. Moser and I. C. Trevena, The crystal structure of tin(II) iodide, *Acta Crystallogr., Sect. B*, 1972, **28**, 2965–2971.

52 J. Fenner, Die Kristallstruktur des Zinnsulfidjodids, *Naturwissenschaften*, 1976, **63**, 244.

53 N. E. Brese and M. O'Keeffe, Bond-valence parameters for solids, *Acta Crystallogr., Sect. B*, 1991, **47**, 192–197.

54 I. D. Brown, *The Chemical Bond in Inorganic Chemistry: the Bond Valence Model*, Oxford University Press, 2006.

55 J. Fenner, Die Kristallstruktur des Zinnsulfidiodids Sn_4 S I_6, *Z. Anorg. Chem.*, 1978, **33**, 479–481.

56 B. Krebs, Die Kristallstrukturen von Pb_4SeBr_6, $Pb_5S_2I_6$ und $Pb_7S_2Br_{10}$, *Z. Anorg. Allg. Chem.*, 1973, **396**, 137–151.

57 S. M. Islam, C. D. Malliakas, D. Sarma, D. C. Maloney, C. C. Stoumpos, O. Y. Kontsevoi, A. J. Freeman and M. G. Kanatzidis, Direct Gap Semiconductors $Pb_2BiS_2I_3$, $Sn_2BiS_2I_3$, and Sn_2BiSI_5, *Chem. Mater.*, 2016, **28**, 7332–7343.

58 M. Ohmasa and K. Mariolacos, The crystal structure of $(Pb_{1-x},Bi_x)Bi_2Cu_2Cu_{2-x}S_5I_2$ (x = 0.88), *Acta Crystallogr., Sect. B*, 1974, **30**, 2640–2643.

59 T. Balić-Žunić, K. Mariolacos, K. Friese and E. Makovicky, Structure of a synthetic halogen sulfosalt, Cu_3 Bi_2 S_3 I_3, *Acta Crystallogr. B*, 2005, **61**, 239–245.

60 A. Heerwig, A. Isaeva and M. Ruck, Copper(I) d10···d10 Interactions and Diselenide(1–) Radical Anions in Mixed Valent Selenides Cu4–BiSe4I, *Z. Anorg. Allg. Chem.*, 2011, **637**, 1131–1136.

61 A. Audzijonis, R. Žaltauskas, R. Sereika, L. Žigas and A. Rėza, Electronic structure and optical properties of BiSI crystal, *J. Phys. Chem. Solids*, 2010, **71**, 884–891.

62 A. Kikuchi, Y. Oka and E. Sawaguchi, Crystal Structure Determination of SbSI, *J. Phys. Soc. Jpn.*, 1967, **23**, 337–354.

63 T. Rosenthal, M. Döblinger, P. Wagatha, C. Gold, E.-W. Scheidt, W. Scherer and O. Oeckler, Structural Features and Physical Properties of $In_2Bi_3Se_7I$, $InBi_2Se4I$, and BiSeI, *Z. Anorg. Allg. Chem.*, 2011, **637**, 2239–2245.

64 P. Kubelka and F. Munk, Ein Beitrag zur Optik der Farbanstriche, *Z. Für Techn Phys.*, 1931, **12**, 593–601.

65 P. Makuła, M. Pacia and W. Macyk, How To Correctly Determine the Band Gap Energy of Modified Semiconductor Photocatalysts Based on UV–Vis Spectra, *J. Phys. Chem. Lett.*, 2018, **9**, 6814–6817.

66 J. Tauc, R. Grigorovici and A. Vancu, Optical Properties and Electronic Structure of Amorphous Germanium, *Phys. Status Solidi B*, 1966, **15**, 627–637.

67 W. Peng, L. Li, S. Yu, H. Zheng and P. Yang, Structure, binding energy and optoelectrical properties of p-type CuI thin films: The effects of thickness, *Appl. Surf. Sci.*, 2020, **502**, 144424.

68 M. Nakamura, S. Inagaki, Y. Okamura, M. Ogino, Y. Takahashi, K. Adachi, D. Hashizume, Y. Tokura and M. Kawasaki, Band structures in orientation-controlled CuI thin films under epitaxial strain, *Phys. Rev. B*, 2022, **106**, 125307.

69 M. T. Hörantner, T. Leijtens, M. E. Ziffer, G. E. Eperon, M. G. Christoforo, M. D. McGehee and H. J. Snaith, The Potential of Multijunction Perovskite Solar Cells, *ACS Energy Lett.*, 2017, **2**, 2506–2513.

70 C. Adamo and V. Barone, Toward reliable density functional methods without adjustable parameters: The PBE0 model, *J. Chem. Phys.*, 1999, **110**, 6158–6170.

71 A. V. Krukau, O. A. Vydrov, A. F. Izmaylov and G. E. Scuseria, Influence of the exchange screening parameter on the performance of screened hybrid functionals, *J. Chem. Phys.*, 2006, **125**, 224106.

72 S. E. Gant, J. B. Haber, M. R. Filip, F. Sagredo, D. Wing, G. Ohad, L. Kronik and J. B. Neaton, Optimally tuned starting point for single-shot *GW* calculations of solids, *Phys. Rev. Mater.*, 2022, **6**, 053802.

73 H. A. Huy, B. Aradi, T. Frauenheim and P. Deák, Calculation of carrier-concentration-dependent effective mass in Nb-doped anatase crystals of TiO_2, *Phys. Rev. B*, 2011, **83**, 155201.

74 J. Tang, L. Y. Deng, C. B. Tay, X. H. Zhang, J. W. Chai, H. Qin, H. W. Liu, T. Venkatesan and S. J. Chua, Determination of carrier concentration dependent electron effective mass and scattering time of n-ZnO thin film by terahertz time domain spectroscopy, *J. Appl. Phys.*, 2014, **115**, 033111.

75 A. Mavlonov, T. Razykov, F. Raziq, J. Gan, J. Chantana, Y. Kawano, T. Nishimura, H. Wei, A. Zakutayev, T. Minemoto, X. Zu, S. Li and L. Qiao, A review of Sb_2Se_3 photovoltaic absorber materials and thin-film solar cells, *Sol. Energy*, 2020, **201**, 227–246.

76 N. T. Hahn, J. L. Self and C. B. Mullins, BiSI Micro-Rod Thin Films: Efficient Solar Absorber Electrodes?, *J. Phys. Chem. Lett.*, 2012, **3**, 1571–1576.

77 T. J. Whittles, *Electronic Characterisation of Earth-Abundant Sulphides for Solar Photovoltaics*, Springer International Publishing, Cham, 2018.

78 J. W. Pinder, G. H. Major, D. R. Baer, J. Terry, J. E. Whitten, J. Čechal, J. D. Crossman, A. J. Lizarbe, S. Jafari, C. D. Easton, J. Baltrusaitis, M. A. van Spronsen and M. R. Linford, Avoiding common errors in X-ray photoelectron spectroscopy data collection and analysis, and properly reporting instrument parameters, *Appl. Surf. Sci. Adv.*, 2024, **19**, 100534.

79 L. R. V. Buizza, H. C. Sansom, A. D. Wright, A. M. Ulatowski, M. B. Johnston, H. J. Snaith and L. M. Herz, Interplay of Structure, Charge-Carrier Localization and Dynamics in Copper-Silver-Bismuth-Halide Semiconductors, *Adv. Funct. Mater.*, 2022, **32**, 2108392.

80 S. Lal, M. Righetto, B. W. J. Putland, H. C. Sansom, S. G. Motti, H. Jin, M. B. Johnston, H. J. Snaith and L. M. Herz, The Role of Chemical Composition in Determining the Charge-Carrier Dynamics in $(AgI)_x(BiI_3)_y$ Rudorffites, *Adv. Funct. Mater.*, 2024, **34**, 2315942.

81 M. Righetto, Y. Wang, K. A. Elmestekawy, C. Q. Xia, M. B. Johnston, G. Konstantatos and L. M. Herz, Cation-Disorder Engineering Promotes Efficient Charge-Carrier Transport in AgBiS2 Nanocrystal Films, *Adv. Mater.*, 2023, **35**, 2305009.

82 V. J.-Y. Lim, A. M. Ulatowski, C. Kamaraki, M. T. Klug, L. Miranda Perez, M. B. Johnston and L. M. Herz, Air-Degradation Mechanisms in Mixed Lead-Tin Halide Perovskites for Solar Cells, *Adv. Energy Mater.*, 2023, **13**, 2200847.

83 (*a*) CCDC 2503028: Experimental Crystal Structure Determination, 2026, DOI: 10.25505/fiz.icsd.cc2q0lv6; (*b*) CCDC 2503027: Experimental Crystal Structure Determination, 2026, DOI: 10.25505/fiz.icsd.cc2q0lt5.